A Chemosensor of 1,8-Dihydroxyanthraquinone PMOs Prepared in a Ternary Deep Eutectic Solvent for the Sensitive Detection of Cu²⁺

Zhi Li and Shuhua Han*

ACCESS | 📊 Metrics & More | 📄 Article Recommendations | 🗒️ Supporting Information

ABSTRACT: A novel type of organic−inorganic hybrid periodic mesoporous materials based on 1,8-dihydroxyanthraquinone (DHAQ-PMOs) was synthesized in a ternary deep eutectic solvent (DES). In the process of the material synthesis, an organosiloxane precursor (DHAQ-Si) and tetraethylorthosilicate (TEOS) were used as the mixed Si source, and cetyltrimethylammonium bromide (CTAB) was used as the structure directing agent. The DES formed by choline chloride (ChCl), urea (U), and ethylene glycol (EG) was used as a green solvent. The water needed for the hydrolysis of DHAQ-Si and TEOS was provided from free water in the sodium hydroxide solution. As characterized by small-angle X-ray scattering, nitrogen adsorption/desorption isotherms, and high-resolution transmission electron microscopy, the obtained mesoporous materials exhibit a two-dimensional hexagonal (*P6mm*) structure. DHAQ possesses double fluorescence emission peaks at *ca.* 520 and 580 nm due to the effect of the excited-state intramolecular proton transfer (ESIPT). For DHAQ-PMOs, the silica framework can provide a rigid environment that makes the fluorescence properties more stable and the fluorescence emission peak appears to red-shift obviously. The DHAQ-PMOs have high selectivity and sensitivity in a wide pH range that can be used to detect Cu²⁺, and the limit of detection (LOD) is as low as 2.39×10^{-9} M. Fluorescence polarization experiments, high-resolution mass spectrometry, and Fourier transform infrared spectroscopy were used to study the coordination interaction between DHAQ and Cu²⁺. The density functional theory (DFT) was used to further prove the coordination ability and interaction between DHAQ and Cu²⁺. XPS spectra were also done to prove the coordination of DHAQ and DHAQ-PMO-10 with Cu²⁺. In addition, confocal fluorescence microscope images exhibit that DHAQ-PMOs can detect Cu²⁺ in living cells. The results show that DHAQ-PMOs have great application potential as a sensor for the detection of Cu²⁺.
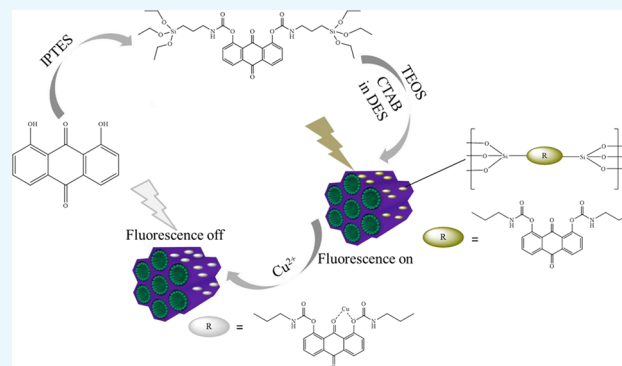
1. INTRODUCTION

Mesoporous silica has a tunable pore size, controllable pore structure, and large surface area.[1] The introduction of organic groups, which were embedded in the framework through covalent bonds, makes periodic mesoporous organosilicas (PMOs) not only have the excellent characteristic of mesoporous materials but also have the unique properties of organic groups. Active sites provided by organic groups make PMOs have a wide range of applications, such as catalysis,[2−4] adsorption,[5−7] drug delivery,[8,9] sensing,[10,11] and so on. Especially, PMO materials have been used as fluorescence sensors to detect many metal ions, such as Cu²⁺,[12] Co²⁺,[13] Zn²⁺,[14] *etc.* Our group synthesized PMOs based on rhodamine-6G Schiff derivative-bridged organosilanes (RS-Si), a bis-(rhodamine Schiff-base derivative) bridged precursor with four silyl groups (BRH-Si₄), and a (tetraylnitrilomethylidyne-hexaphenyl (TH))-derived tetrasiloxane precursor (TH-Si₄), respectively.[15−17] These PMOs show excellent fluorescence properties and good optical stability and can be used to specifically detect Cu²⁺. Kaczmarek and Van Der Moort synthesized PMOs based on *N,N*-bis(trimethoxysilylpropyl)-

2,6-pyridine dicarboxamide and grafted with lanthanides, which show a selective response to Pb²⁺ and Cr³⁺.[18] Wang *et al.* synthesized PMOs by covalently binding Schiff base 3-((4-aminophenyl)imino)-5-fluoroindolin-2-one (APIFI) with ep-oxypropoxyl groups in the siliceous walls to detect Sn²⁺ with high selectivity and sensitivity.[19]

Quinones have a highly conjugated structure and show different colors, so they are often found in nature as pigments in animals, plants, and microorganisms. 1,8-Dihydroxyanthra-quinone (DHAQ) is a member of the anthraquinones and usually found in some dyes and industrial raw materials.[20] DHAQ is a highly conjugated compound with two hydroxyl groups at positions 1 and 8 and two quinone bonds at
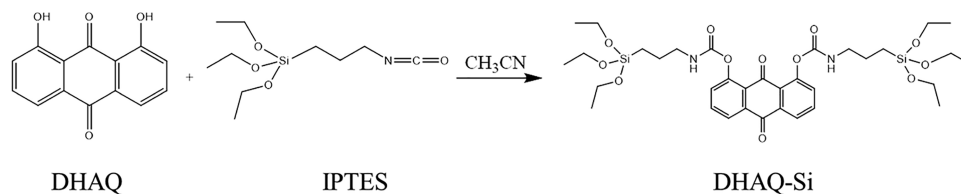
Scheme 1. The Schematic Diagram of the Synthesis Process of DHAQ-Si

DHAQ   IPTES   DHAQ-Si

Scheme 2. The Schematic Diagram of the Synthesis Process of DHAQ-PMOs
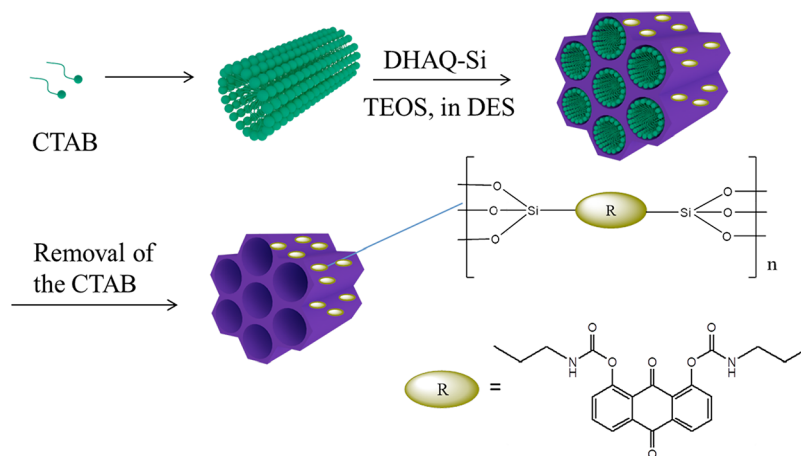
positions 9 and 10 in the anthraquinous ring, which can emit fluorescence under ultraviolet light based on the excited-state intramolecular proton transfer (ESIPT) and intramolecular charge transfer (ICT) fluorescence emission mechanisms. There are also many fluorescence emission mechanisms that have been reported by researchers, such as photoinduced electron transfer (PET), chelation-enhanced fluorescence (CHEF), and so on. Yan *et al.* synthesized a novel fluorescence probe, N'-((1-hydroxynaphthalen-2-yl)methylene)-isoquinoline-3-carbohydrazide (NHMI), based on the ESIPT and PET mechanisms, which showed a distinctive "turn-on" fluorescence signal toward Al^{3+} and Mg^{2+}.[21] Yadav *et al.* designed and developed a new chemical sensor to monitor the fluoride in water. This sensor showed a "turn-off" fluorescence response toward F^- due to the enhanced PET and ICT process with a low limit of detection.[22] Zhang *et al.* designed a new multiresponse pyrazoline-based fluorescent sensor, which exhibited high sensitivity for detecting Zn^{2+} and Cd^{2+} in an ethanol aqueous solution based on the ICT and CHEF effects.[23]

Deep eutectic solvents (DESs) are a new type of solvent that are gradually replacing toxic organic reagents. The concept of DESs was first described by Abbott *et al.* in 2003.[24] DESs are composed of a hydrogen bond donor (HBD) and hydrogen bond acceptor (HBA) through hydrogen bond interactions with a much lower melting point than any individual component.[25] For DESs themselves, their toxicity is nonexistent or very low, and their biodegradability and biocompatibility are good,[26−28] which make them environmentally benign alternatives for synthesis. Most DESs are liquid and can be stored at room temperature, but the viscosity is higher. Therefore, a ternary DES composed of choline chloride (ChCl), urea (U), and ethylene glycol (EG) is utilized as the solvent for the preparation of PMOs, in which the viscosity of the DES is lower than that of ordinary DESs. Recently, some researchers have used DES as the templating

agent to synthesize mesoporous materials. For instance, Lee *et al.* reported a new method for synthesizing mesoporous materials using the DES of ChCl/U as the solvent and templating agent.[29] Ferreira *et al.* also synthesized mesoporous polysaccharide/sol−gel composites with ChCl-based DESs as the templating agents.[30]

Here, a new periodic mesoporous organosilica material (DHAQ-PMO) was prepared in the ternary DES of ChCl/U/EG. First of all, DHAQ and 3-isocyanatopropyltriethoxysilane (IPTES) were used to form the organosiloxane precursor (DHAQ-Si) (Scheme 1). Then, in alkaline conditions of the DES, DHAQ-PMOs were prepared through hydrolysis and polycondensation, in which DHAQ-Si and tetraethyl orthosilicate (TEOS) were the mixed silicon sources and cetyltrimethylammonium bromide (CTAB) was the structure directing agent. The water needed for the hydrolysis of DHAQ-Si and TEOS was provided from free water in the sodium hydroxide solution. Subsequently, in the ternary DES, thermal treatment was carried out in a sealed reactor at an elevated temperature, in which the internal pressure of the sealed reactor was lower than that under thermal treatment conditions using lots of water and other solvents.[29] Therefore, DES provides a method for the synthesis procedure with higher safety and economic feasibility. The resulting hybrid mesoporous silica was modified by DHAQ groups that were grafted into the mesoporous silica pore walls (Scheme 2). Moreover, DHAQ-PMOs exhibit a good mesoporous structure and excellent fluorescence properties, which can be used to detect Cu^{2+} with high selectivity and high sensitivity. The limit of detection (LOD) can be as low as the nanomolar concentration range. To the best of our knowledge, there are no reports on the use of the ternary DES for the synthesis of PMO bridged DHAQ as a solid chemosensor to detect Cu^{2+}.
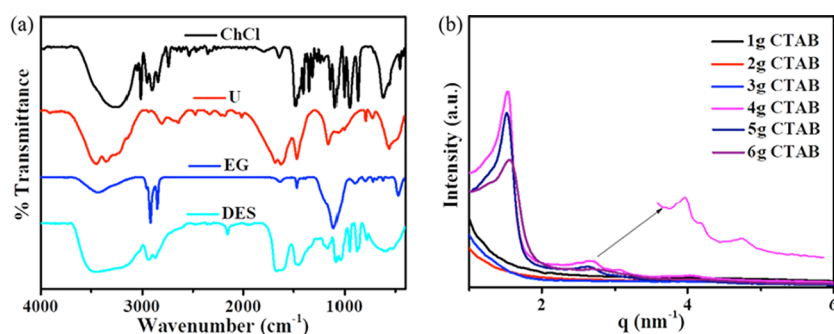
Figure 1. (a) The FTIR spectra of the ternary DES prepared by ChCl/U/EG. (b) The SAXS pattern of inorganic mesoporous materials prepared with different contents of CTAB.
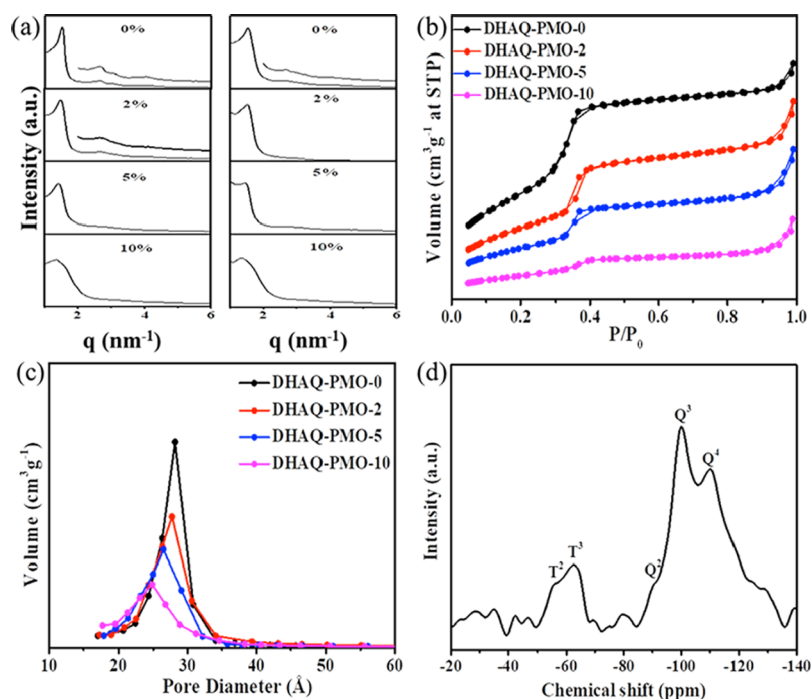

Figure 2. (a) SAXS patterns of DHAQ-PMOs (left) before and (right) after the extraction of CTAB. (b) N_2 adsorption/desorption isotherms and (c) pore size distribution curves of DHAQ-PMO-X (X = 0, 2, 5, 10). (d) ^{29}Si MAS NMR spectrum of DHAQ-PMO-10.

2. RESULTS AND DISCUSSION

2.1. The FTIR Spectra of DES, DHAQ, DHAQ-Si, and DHAQ-PMOs. The hydrogen bond network exists in the DES due to U and EG together as the co-HBD and ChCl as the HBA. Figure 1a shows the FTIR spectra of the ternary DES system. The DES has a broad and high intensity band between 3700 and 3000 cm^{-1}, which belongs to the intramolecular hydrogen bond. The peaks at 2941 and 2876 cm^{-1} belong to the stretching vibration of saturated alkanes in the ternary DES. The peaks at 1624 and 1620 cm^{-1} can be assigned to the stretching vibration of $-C=O$ and the bending vibration of $-N-H$. The peak at 1451 cm^{-1} can be ascribed to the C−N stretching vibration. For ChCl, the broad peak at 3255 cm^{-1} is assigned to the stretching vibration of −OH. The peaks below 3000 cm^{-1} belong to the −C−H stretching vibration of saturated alkanes. The peaks at 1477 and 1090 cm^{-1} belong to the C−N stretching vibration and the −CH_2 rocking vibration.[31] For U, the saddle-shaped peaks at 3445 and 3349 cm^{-1} are attributed to the stretching vibration of −NH_2 in the molecule. The peaks at 1680 and 1616 cm^{-1} belong to the stretching vibration of −C=O and the bending vibration

of −NH. The peak at 1464 cm^{-1} can be ascribed to the C−N stretching vibration.[32] As for EG, the stretching vibration of −OH is at 3435 cm^{-1}. The symmetric and antisymmetric stretching vibration peaks of −CH_2− are at 2950 and 2880 cm^{-1}. The peak at 1106 cm^{-1} belongs to the −COH stretching vibration.[33] When the ternary DES is formed, blue-shifts are observed for the stretching vibration peak of −OH in ChCl and the stretching vibration and bending vibration of −NH_2 in U. At the same time, the intensity of the −OH in EG is enhanced, which indicated that they are all involved in the formation of the large number of hydrogen bonds (N−H···Cl, O−H···O, O−H···Cl, etc.) in the DES.[34,35]

The FTIR spectra of DHAQ, DHAQ-Si, and DHAQ-PMOs are shown in Figure S1a. The characteristic peaks of DHAQ are displayed at 3073 and 1627 cm^{-1}, which correspond to the −OH stretching vibration and −C=O stretching vibration. The characteristic peaks at 3353, 2900−2800, 1634, 1560, 1093, and 772 cm^{-1} of DHAQ-Si belong to the −NH stretching vibration, −CH stretching vibration, −C=O stretching vibration, −NH bending vibration, −C−N stretching vibration, and −CH out-of-plane bending vibration, respec-

Table 1. Mesoporous Structure Properties of DHAQ-PMOs

sample	q (nm^{-1})	d_{100} (nm)	a_0 (nm)[a]	S_{BET} (m^2 g^{-1})[b]	V_t (cm^3 g^{-1})[c]	D_{BJH} (nm)[d]	b (nm)[e]
DHAQ-PMO-0	1.53	4.10	4.73	1098	1.03	2.82	1.91
DHAQ-PMO-2	1.48	4.24	4.90	739	0.86	2.77	2.13
DHAQ-PMO-5	1.41	4.45	5.14	530	0.65	2.65	2.49
DHAQ-PMO-10	1.35	4.65	5.37	250	0.35	2.48	2.89

[a]a_0: lattice parameter. [b]S_{BET}: BET surface area. [c]V_t: total pore volume. [d]D_{BJH}: pore diameter, calculated from the absorption branches by the BJH method. [e]b: wall thickness, $b = a_0 - D_{BJH}$, where $a_0 = 2d(100)/\sqrt{3}$.

tively. Compared to those of DHAQ and DHAQ-Si, the DHAQ-PMOs show bands at 3446, 3000−2900, 1630, 1560, 1073, and 798 cm^{-1}. The band at 3446 cm^{-1} is assigned to the stretching vibration of −SiOH. The bands between 3000 and 2900 cm^{-1} are attributed to the aliphatic C−H stretching vibration. The bands at 1630 and 1560 cm^{-1} are due to the stretching vibration of the −C≡O bond and the bending vibration of the −NH bond. The peaks at 1073 and 798 cm^{-1} are attributed to the Si−O−Si stretching vibration and Si−O frameworks.[36] These results indicate that DHAQ-Si has been successfully introduced into the pore walls of DHAQ-PMOs.

2.2. ¹H NMR of the Ternary DES. ¹H NMR was used to further characterize the hydrogen bond network in the ternary DES (Figure S2). The chemical shifts of −OH in EG and −NH$_2$ in U move downfield (at 4.00 and 6.04 ppm, respectively), and the chemical shift of −OH in ChCl moves upfield to 5.07 ppm.[37,38] This phenomenon means that the intramolecular hydrogen bonds between Cl$^-$ and −OH in ChCl are weakened, while intermolecular hydrogen bonds between Cl$^-$ and −OH in EG and −NH$_2$ in U are formed.[39] These results imply that they are involved in the formation of the hydrogen bond network in the DES.

2.3. Effect of CTAB in the Ternary DES on the Pore Structure. Studies have shown that when the concentration of the surfactant in ChCl/glycerol and ChCl/EG is above 45%, a hexagonal liquid crystal phase is formed.[40] Figure 1b shows the effect of CTAB contents on the structure of mesoporous materials in the ternary DES by small-angle X-ray scattering (SAXS). When the content of CTAB in the DES is low, there is no scattering peak in the small angle range (<10), indicating the existence of only a micellar phase in the DES. However, at 4 g of CTAB, that is, the mass fraction of CTAB in the system is up to 42%, there are four scattering peaks that appear in the small angle range. These peak positions meet the ratio of $1:\sqrt{3}:2:\sqrt{7}$ corresponding to the four crystal planes (100), (110), (200), and (210), respectively, which demonstrate the formation of mesoporous materials with a two-dimensional hexagonal (P6mm) structure. With the increase of CTAB content, the third peak on the SAXS pattern fades away and the fourth becomes blurry. These indicate that the mesoporous structural ordering of the mesoporous materials gradually decreases.

2.4. Mesoporous Structure and Morphology of DHAQ-PMOs. The SAXS patterns of DHAQ-PMOs before and after extraction of CTAB are shown in Figure 2a, which was used to characterize the pore structure of DHAQ-PMOs. As we can see from the figure, all the materials show scattering peaks in the small angle range. It demonstrates that these materials have formed an ordered mesoporous structure. For DHAQ-PMO-0, there are four scattering peaks at 1.53, 2.66, 3.08, and 4.03 nm^{-1}, respectively. These peak positions meet the ratio of $1:\sqrt{3}:2:\sqrt{7}$ corresponding to the four crystal planes (100), (110), (200), and (210), respectively, which

indicate the formation of a P6mm structure. As for DHAQ-PMO-2, there are two peaks at 1.48 and 2.56 nm^{-1}, which conform to the ratio of $1:\sqrt{3}$. The result shows that DHAQ-PMO-2 also has a P6mm structure. With the increase of DHAQ-Si content in the mixed silica source, the scattering peaks of materials gradually broaden and the intensity gradually decreases, the scattering peaks corresponding to the (200) and (210) crystal plane gradually disappear, and the scattering peak corresponding to the (110) crystal plane is blurred, which means that the degree of order of the mesoporous structure of DHAQ-PMOs is greatly reduced. In addition, the q values assigned to the (100) crystal planes of DHAQ-PMO-0, DHAQ-PMO-2, DHAQ-PMO-5, and DHAQ-PMO-10 are 1.53, 1.48, 1.41, and 1.35 nm^{-1}. And the d-spacing values are 4.10, 4.24, 4.45, and 4.65 nm calculated from q values. The d-spacing values gradually increase with the addition of the DHAQ-Si content. It illustrates that the pore walls are gradually thicker to overcome the increase of the DHAQ-Si content in the DHAQ-PMOs.[41] The mesoporous structure of the materials can still be maintained after the surfactant is extracted.

To investigate the pore structure properties of DHAQ-PMOs, the nitrogen adsorption/desorption isotherms are shown in Figure 2b. All these materials show type IV adsorption/desorption isotherms and obvious H$_1$ hysteresis loops, which are the typical characteristics of mesoporous materials.[42] The production of H$_1$ hysteresis loops is due to the capillary condensation of nitrogen in the cylindrical mesopores.[43] In addition, Figure 2c shows uniform and narrow pore size distributions of DHAQ-PMOs. The mesoporous structure properties are shown in Table 1. The surface areas (S_{BET}) are calculated by the Brunauer−Emmett−Teller (BET) method, and pore sizes are calculated by the Barrett−Joyner−Halenda (BJH) method through the branching of the absorption curves, respectively. From Table 1, it can be concluded that the specific surface area, pore volume, and pore diameter decrease with the addition of the DHAQ-Si content. The reason for this phenomenon is that the organosiloxane precursors are embedded in the pore wall of the materials and occupy a certain channel.[5] These results show that DHAQ-Si has been successfully bonded to the materials and reduced the ordering of the mesopore structure to some extent.

Solid-state ²⁹Si MAS NMR measurement was used to further characterize the condensation degree and silicon environment in the silica framework of the DHAQ-Si (Figure 2d). DHAQ-PMO-10 exhibits two types of signals from −50 to −67 and from −84 to −134 ppm, respectively. The signal peaks at −55 and −62 ppm are respectively attributed to silicon resonances of T^2 and T^3 (T^n: RSi$(OSi)_n(OH)_{3-n}$, R: organic group) sites, which are due to the hydrolysis and polycondensation between DHAQ-Si and TEOS, while the signal peaks at −90, −100, and −110 ppm correspond to Q^2, Q^3, and Q^4 (Q^n: Si-$(OSi)_n(OH)_{4-n}$), respectively. These results indicate that the
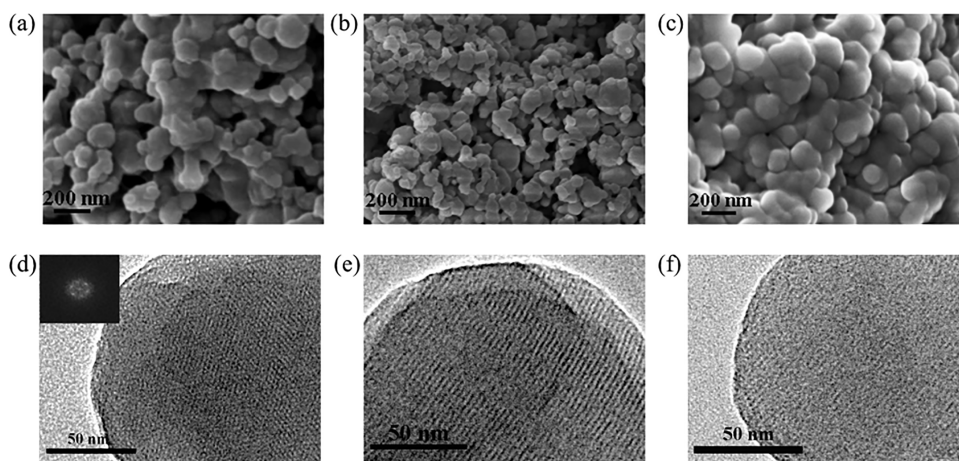
Figure 3. The (a, b, c) SEM and (d, e, f) HRTEM images of (a, d) DHAQ-PMO-2, (b, e) DHAQ-PMO-5, and (c, f) DHAQ-PMO-10 after the extraction of CTAB. Inset is the Fourier transform pattern image of the HRTEM.
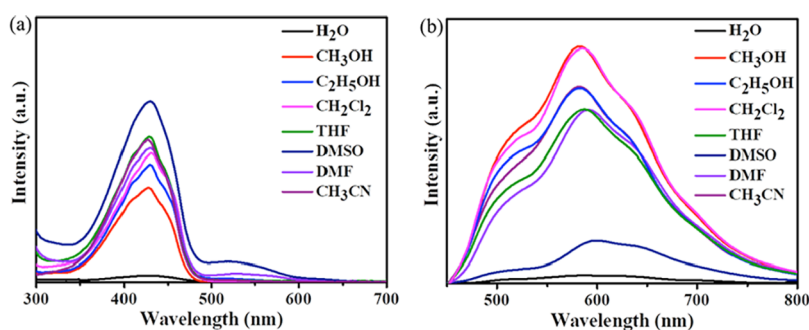

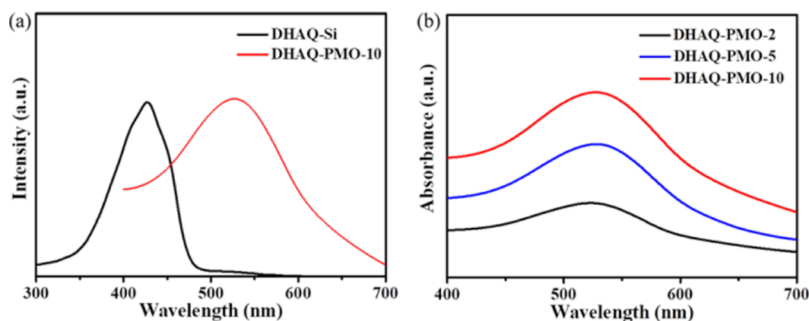**Figure 4.** (a) The UV−vis absorption and (b) fluorescence emission spectra of DHAQ in different solvents.

Figure 5. (a) The UV−vis absorption spectrum of DHAQ-Si in the CH_3OH solution and UV−vis diffuse reflectance spectrum of DHAQ-PMO-10. (b) UV−vis diffuse reflectance spectra of DHAQ-PMO-2, DHAQ-PMO-5, and DHAQ-PMO-10.

DHAQ-Si has been successfully incorporated into the frameworks of PMOs through Si−O covalent bonds.[44]

Figure S1b shows the TGA and DSC curves of DHAQ-PMO-10. The data are used to comprehend the thermal stability of this material. There are four main mass losses. The first mass loss of about 6.5% below 120 °C is due to the loss of physically adsorbed water. The second weight loss of about 7% between 120 and 200 °C is attributed to the elimination of crystal water. The decomposition of organic groups in the sample occurs from 200 to 340 °C. The quality loss of this part is about 16%. The last mass loss between 340 and 800 °C of about 10% corresponds to the further condensation of residual silanol to form the Si−O−Si network. These data prove that the sample can maintain good thermal stability up to 200 °C.

Figure 3 exhibits the SEM and HRTEM images of DHAQ-PMO-2, DHAQ-PMO-5, and DHAQ-PMO-10 to show the

structural characteristics of the materials more intuitively. In Figure 3a−c, the materials are spherical particles in shape with a regular structure and the average particle diameter is about 150 nm. However, with the increase of the DHAQ-Si content, the shape gradually becomes irregular and the particles are aggregated together. Figure 3d−f clearly shows a mesoporous structure with ordered mesoporous channels of about 2.60 nm. The hexagonal diffraction points of the (100) crystal plane can prove the existence of space group *P6mm* of the mesoporous structure (Figure 3d inset). In the same way, as the content of DHAQ-Si increases, the shape of the channels of the material becomes disordered, but the mesoporous channels still exist.

2.5. Optical Properties of DHAQ, DHAQ-Si, and DHAQ-PMOs. The optical properties of DHAQ, DHAQ-Si, and DHAQ-PMO-10 were studied by UV−vis absorption and fluorescence emission spectra (Figure 4, Figures S3 and S4).
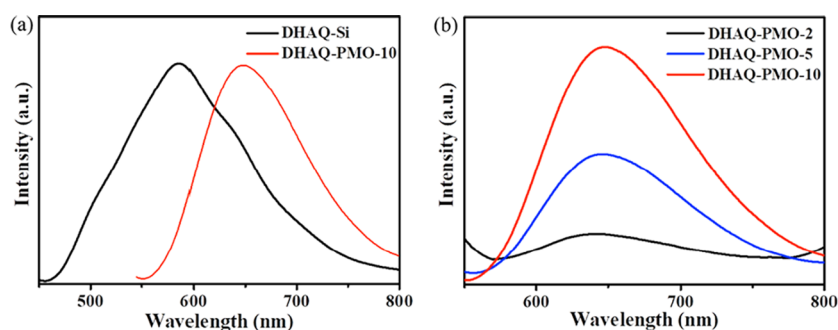
Figure 6. Fluorescence emission spectra in the CH$_3$OH solution of (a) DHAQ-Si and DHAQ-PMO-10. (b) DHAQ-PMO-2, DHAQ-PMO-5, and DHAQ-PMO-10.
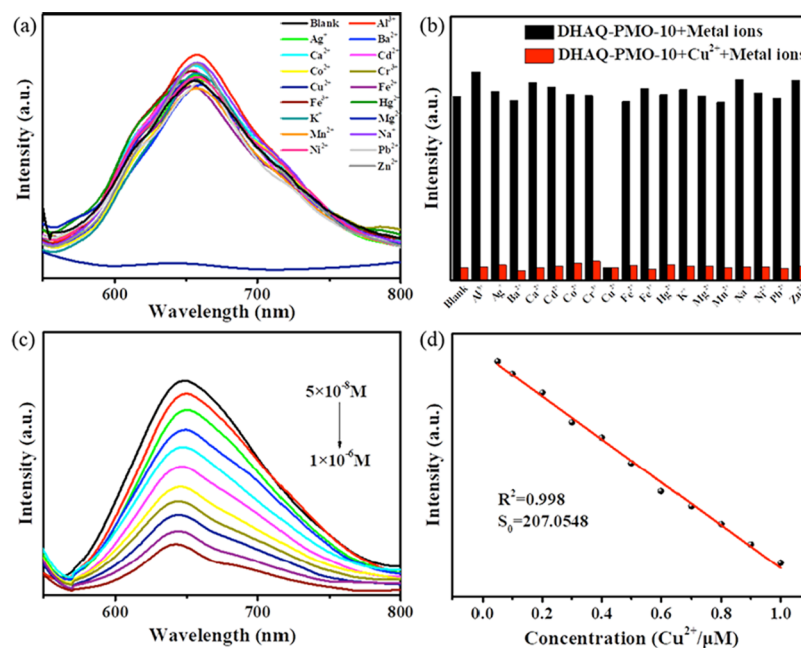

Figure 7. Fluorescence emission spectra of DHAQ-PMO-10 (10^{-4} g/mL) in the CH$_3$OH/H$_2$O (1:9, v/v, 10 mM HEPES buffer, pH = 7.4) solution with (a) different metal ions (10^{-5} M). (b) Single different metal ion (black bar) and in the mixture of Cu^{2+} and other metal ions (red bar). (c) Different concentrations of Cu^{2+} (5 × 10^{-8}−1 × 10^{-6} M). (d) Linear relationship between fluorescence intensities at 656 nm of DHAQ-PMO-10 (10^{-4} g/mL) and the concentration of Cu^{2+}.

DHAQ has a broad absorption band at 432 nm with the shoulder peak at 400 nm, which belongs to the n → π* electronic transition in Figure 4a.[45] There are double fluorescence emission peaks at *ca.* 520 and 580 nm, which are attributed to the keto and enol emission of DHAQ (Figure 4b), respectively, due to the ESIPT effect. Because of poor solubility in water, the intensity of UV−vis absorption and fluorescence emission spectra is very low for DHAQ. Figure S3 shows the UV−vis absorption and fluorescence emission spectra of DHAQ-Si in different solvents. They are similar to those of DHAQ compared with each other.

The UV−vis absorption spectra of DHAQ-Si in the CH$_3$OH solution and UV−vis diffuse reflectance spectra of DHAQ-PMOs are shown in Figure 5. A red-shift (~96 nm) from 430 to 526 nm is observed for the absorption band, and the peak shape becomes wider for DHAQ-PMOs compared with that of DHAQ-Si. The reasons for this phenomenon are as follows: On the one hand, it may be attributed to the degree of conjugation or coplanarity of the anthraquinone ring in DHAQ-PMOs being enhanced after the introduction of DHAQ-Si into the silica framework.[46] On the other hand, in

strong alkaline conditions, the nucleophilic addition reaction of hydroxide ions to carbonyl groups of isocyanate moieties in the materials results in a significant increase of the ICT process, producing a significant red-shift in the absorption and fluorescence emission spectra of the materials.[47] In Figure 5b, the intensity of absorption bands is gradually increased with the addition of DHAQ-Si content in the materials, indicating that DHAQ-Si has been successfully anchored into the pore walls of the mesoporous materials. And the shape of absorption bands does not change significantly, which demonstrates that the introduction of DHAQ-Si into mesoporous materials does not affect the molecule structure of DHAQ.

Figure S4 shows the UV−vis absorption and fluorescence emission spectra of DHAQ-PMO-10 in different solvents. In aprotic solvents, the absorption and emission spectra have little change in wavelength. But in protic solvents, such as CH$_3$OH and C$_2$H$_5$OH, the fluorescence emission spectra are obviously red-shifted and have large Stokes shifts (>100 nm). This phenomenon can be explained by the fact that the excited state is more stabilized by intermolecular hydrogen bonding in

protic solvents.[48,49] Based on these reasons, we choose CH_3OH as the follow-up test solvent.

Figure 6 shows the fluorescence emission spectra of DHAQ-Si and DHAQ-PMOs in the CH_3OH solution at room temperature. The emission wavelengths appear at 586 nm for DHAQ-Si and at 648 nm for DHAQ-PMO-10. A large red-shift in wavelength (62 nm) is present for DHAQ-PMO-10 compared to that of DHAQ-Si. The reason for this phenomenon is similar to the red-shift of the UV absorption spectra. Moreover, the fluorescence emission spectra of DHAQ-PMOs do not show any significant change in the shape and position with increasing DHAQ content, which illustrate that the silica skeleton does not influence the fluorescence properties of DHAQ-Si in the excited state. At the same time, the intensity of fluorescence is gradually increased along with the increase of the amount of DHAQ-Si, which attributes that more DHAQ-Si are introduced into the materials, and make the fluorescence emission enhance.

The fluorescence lifetime experiment was performed by time-dependent single photon counting. Figure S5 shows the normalized decay curves of DHAQ-Si and DHAQ-PMOs. The decay curves of all materials can be fitted by a double-exponential equation, which means that two fluorescence decay mechanisms exist in DHAQ-PMOs.[50,51] The short lifetime (τ_1) belongs to the monomer emission, and the long lifetime (τ_2) is produced by the interaction between DHAQ molecules due to a radical complex. For DHAQ-Si, the average lifetime (τ) is 0.74 ns. And as for DHAQ-PMOs, τ is 2.02 ns for DHAQ-PMO-2, 1.60 ns for DHAQ-PMO-5, and 1.29 ns for DHAQ-PMO-10, respectively (Table S1). Also, the fluorescence quantum yields (Φ), fluorescence radiative decay rate constant (k_f), and nonradiative decay rate constant (k_{nr}) of DHAQ-Si and DHAQ-PMOs are listed in Table S1. For DHAQ-Si, Φ is 0.81%, k_f is 1.09×10^7 s^{-1}, and k_{nr} is 13.1×10^8 s^{-1}. Compared with those of DHAQ-Si, Φ, τ, and k_f of DHAQ-PMOs are increased; however, k_{nr} is decreased, which means that the materials can improve the luminescent efficiency of DHAQ after DHAQ molecules are inserted into the framework of PMOs.[52]

2.6. DHAQ-PMO-10 as a Sensor for the Detection of Cu^{2+}. To investigate the fluorescence response of DHAQ-PMO-10 to various metal ions, we selected the solvent used in the testing process first. On the basis of basically maintaining the fluorescence properties, the integrity of the peak shape and the friendliness to the environment are taken into account. The CH_3OH to H_2O ratio of 1:9 was chosen as the solvent for the test (Figure S6). A HEPES buffer was added to the solvent to maintain the pH stability of the solvent during the test. The DHAQ-PMO-10 shows a fluorescence emission peak centered at 656 nm in the CH_3OH/H_2O (1:9, v/v, 10 mM HEPES buffer, pH = 7.4) solution in the absence of any metal ions (blank sample in Figure 7a). Different metal ions were added to the blank sample, respectively, including Ag$^+$, Al^{3+}, Ba^{2+}, Ca^{2+}, Cd^{2+}, Co^{2+}, Cr^{3+}, Cu^{2+}, Fe^{2+}, Fe^{3+}, Hg^{2+}, K$^+$, Mg^{2+}, Mn^{2+}, Na$^+$, Ni^{2+}, Pb^{2+}, and Zn^{2+}. Only Cu^{2+} significantly quenched the fluorescence emission of DHAQ-PMO-10. The fluorescence quenching of DHAQ-PMO-10 may be attributed to the formation of the DHAQ-Cu^{2+} complex. In addition, to study the influence of other interfering metal ions in the detection of Cu^{2+}, we detected the fluorescence emission spectra when Cu^{2+} and other metal ions both exist in the CH_3OH/H_2O (1:9, v/v, 10 mM HEPES buffer, pH = 7.4) solution (Figure 7b). It was found that Cu^{2+} can still quench the fluorescence

emission of DHAQ-PMO-10 even in the presence of other interfering metal ions with little change of the fluorescence intensity. These results show that DHAQ-PMOs have a good selective recognition behavior toward Cu^{2+} in the solution of CH_3OH/H_2O (1:9, v/v, 10 mM HEPES buffer, pH = 7.4) without any interference of other metal ions. To further prove the excellent selectivity of DHAQ-PMOs, higher concentrations of interfering metal ions (10^{-4}, 10^{-3}, and 10^{-2} M) were added to the solution of DHAQ-PMO-10 containing 10^{-5} M Cu^{2+}, and the fluorescence intensities of these solutions were detected (Figure S7). As we can see from the figure, the results exhibit that DHAQ-PMO-10 still has high selectivity for Cu^{2+}. However, the anti-interference ability of the material decreases to some extent when the concentration of interfering metal ions increases, especially when the concentration is in the 10^{-2} M range.

Sensitivity is another very significant parameter to estimate the presentation of a fluorescence chemosensor. We did the titration experiments to study the sensitivity of the chemosensor. By the successive addition of Cu^{2+} to the solution containing DHAQ-PMO-10, the fluorescence emission intensities present a linear decrease with the increase of Cu^{2+} concentration in the range of 5×10^{-8}–1×10^{-6} M (R^2 = 0.998) (Figure 7c,d). The detection limit (LOD) is calculated to be 2.39×10^{-9} M by the equation LOD = $3S_0/k$, where S_0 is the standard deviation of the blank solution and k is the slope of the calibration curve (Figure 7d). Compared with the LOD of the original organic compound DHAQ for Cu^{2+} (1.11×10^{-8} M, Figure S8), the LOD of DHAQ-PMO-10 is lower, which reaches the level of the nanoscale concentration. There are also some sensors that can detect Cu^{2+} in previous reports, but DHAQ-PMOs still have the advantage in terms of LOD (Table S2). The reason for this phenomenon may be due to the silica framework of PMOs that improves the fluorescence emission of DHAQ.

In addition, the applicability of DHAQ-PMO-10 in solutions was studied under different pH values from 1 to 13 (Figure S9). As we can see from these figures, DHAQ-PMO-10 has stable fluorescence properties in the range of pH 3–13. At the same time, Cu^{2+} also shows a sensitive quenching response in this range of pH. Under light stimulation, the fluorescence intensities of DHAQ-PMO-10 are relatively constant within 60 h (Figure S10a). Moreover, DHAQ-PMOs as a fluorescence chemosensor show excellent reversibility (Figure S10b) as confirmed by the alternating addition of Cu^{2+}/EDTA^{2-} to the solution. EDTA^{2-}, known as a hexadentate chelating ligand, can chelate with various metal ions. We did six sets of parallel cycle tests to prove the reproducibility of the materials. When the strong metal chelator EDTA^{2-} was added to the suspension solution, the fluorescence of DHAQ-PMO-10 quenched by Cu^{2+} can be restored to its initial fluorescence, which is due to the formation of a complex between Cu^{2+} and EDTA^{2-} leaving DHAQ-PMO-10 free. Once the Cu^{2+} was added to the suspension solution again, the fluorescence of DHAQ-PMO-10 can still be quenched. After six cycles, the fluorescence intensity of DHAQ-PMO-10 has no significant change. These results show that the DHAQ-PMOs have good stability and cycle reusability for the detection of Cu^{2+}.

2.7. Mechanism of the Combination Interaction between DHAQ-PMOs and Cu^{2+}. The fluorescence polarization experiment was done to prove the coordination of DHAQ-PMOs and Cu^{2+}. A study has proved that the fluorescence polarization value (P) of the probe binding to

Table 2. The Fluorescence Polarization Values of DHAQ-PMO-10/DHAQ-PMO-10 + Cu^{2+}

	$\bar{I}_{VH}$	S^a (I_{VH})	$\bar{I}_{VV}$	S^a (I_{VV})	$\bar{G}$	S^a (G)	$\bar{P}$	S^a (P)
DHAQ-PMO-10	3161.9	42.95	3583.6	58.77	0.88	0.015	0.12	0.017
DHAQ-PMO-10 + Cu^{2+}	224.7	16.21	883.7	39.02	0.25	0.016	0.88	0.015

^{a}S is the standard deviation.
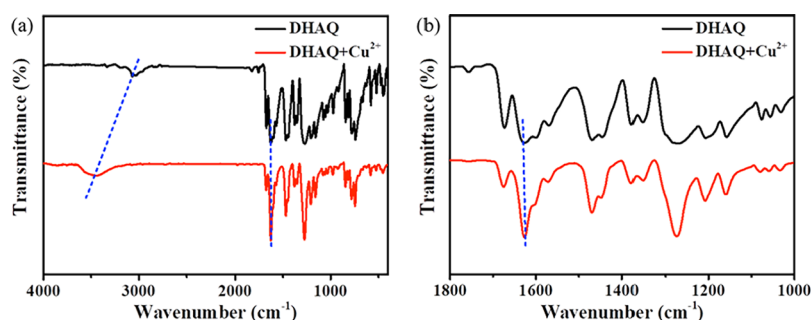
Figure 8. The FTIR spectra of DHAQ (a) before and (b) after adding Cu^{2+}.

the AuNP surface increased significantly in the presence of metal ions.[53] The reason for this phenomenon is that the fluorophore is free in the solution and rotates very fast, and it has a small P value. After forming a complex with metal ions, the rotation speed of the complex decreases, showing a higher P value.[54,55] The P is calculated according to the following equation:

$$P = (I_{VV} - GI_{VH})/(I_{VV} + GI_{VH})$$

where I_{VV} and I_{VH} are the fluorescence intensities of the emission polarizer in the vertical and horizontal direction when the excitation polarizer is in the vertical direction. G is the correction coefficient calculated by $G = I_{HV}/I_{HH}$ (I_{HV} and I_{HH} are the fluorescence intensities in the vertical and horizontal direction with the excitation polarizer in the horizontal direction, respectively).[56] Herein, the P values of DHAQ-PMO-10 and DHAQ-PMO-10 + Cu^{2+} were detected 10 times and then averaged (Table 2). The results show that when Cu^{2+} was added to the DHAQ-PMO-10 solution, the P value actually increases, which indicates that there is a coordination interaction between DHAQ-PMO-10 and Cu^{2+}.

Job's plot experiment was performed to determine the binding ratio between DHAQ and Cu^{2+} (Figure S11). By controlling the total concentration of DHAQ and Cu^{2+} maintained a constant at 1.0×10^{-4} M, change the molar ratio of Cu^{2+} in the total concentration. The fluorescence intensity reaches the minimum emission intensity when the molar faction of Cu^{2+} is 0.5, which indicates that DHAQ and Cu^{2+} form a stable coordination structure with a ratio of 1:1. HRMS can further prove this result (Figure S12). The highest fragment peak at 282.28 is derived from [DHAQ-2H$^+$ + Cu^{2+} − H$_2$O], and the small peak at 318.30 belongs to [DHAQ-2H$^+$ + Cu^{2+} + H$_2$O]. Thus, the molar ratio of DHAQ to Cu^{2+} is 1:1 according to the m/z values of the two fragment peaks.

To determine binding sites between DHAQ and Cu^{2+}, the FTIR spectra of DHAQ and DHAQ-Cu^{2+} are shown in Figure 8. The FTIR spectra of DHAQ before and after the addition of Cu^{2+} change a lot. The band at 3073 cm^{-1} of the hydroxyl group of DHAQ shifts to 3462 cm^{-1}. The band at 1627 cm^{-1} of the carbonyl group shifts to 1623 cm^{-1} upon the addition of Cu^{2+}, and the band shape further becomes sharper, ascribed to the vibration of the compound being limited by the introduction of Cu^{2+}.[57] Thus, it can be inferred that DHAQ may coordinate with Cu^{2+} through phenolic hydroxyl oxygen and carbonyl oxygen atoms of DHAQ.

DFT calculations were also performed to further understand the binding mode of DHAQ and Cu^{2+}. The Gaussian 09 software package was used, and the theoretical level was B3LYP/6-31+G(d, p). The optimized geometry, the highest occupied molecular orbital (HOMO), and the lowest unoccupied molecular orbital (LUMO) of DHAQ and DHAQ-Cu^{2+} are presented in Figure 9. For DHAQ, the
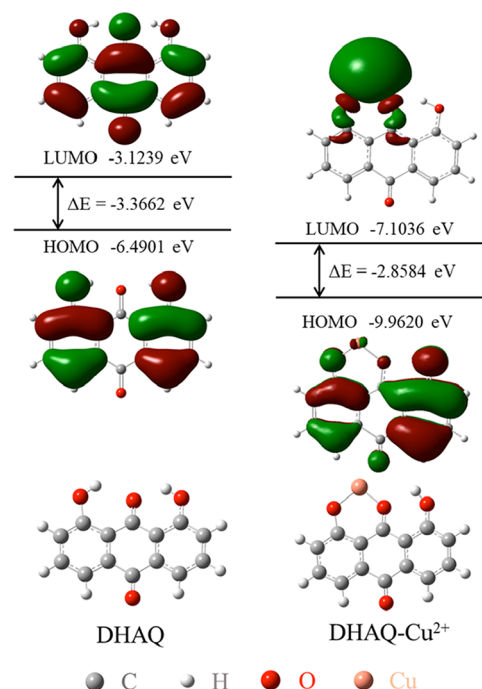
Figure 9. The DFT calculation results from B3LYP/6-31+G(d, p).

electron cloud transfers to the electron-deficient carbonyl group and anthraquinone ring (LUMO) from the hydroxyl group and its benzene ring (HOMO), which suggests that there exists an ICT effect. After coordination with Cu^{2+}, the electron cloud on the HOMO of DHAQ is partially transferred to the carbonyl group and Cu^{2+}; however, the electron cloud on the LUMO is mostly transferred to Cu^{2+} and the two oxygen atoms involved in the coordination. When DHAQ is coordinated with Cu^{2+}, the energy gap of DHAQ-Cu^{2+}
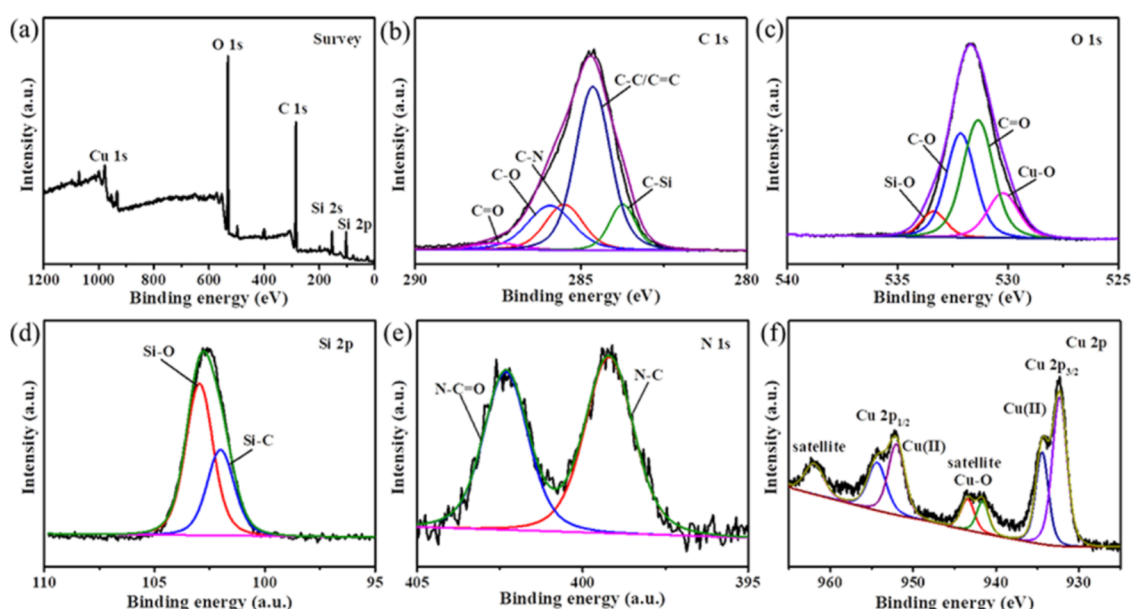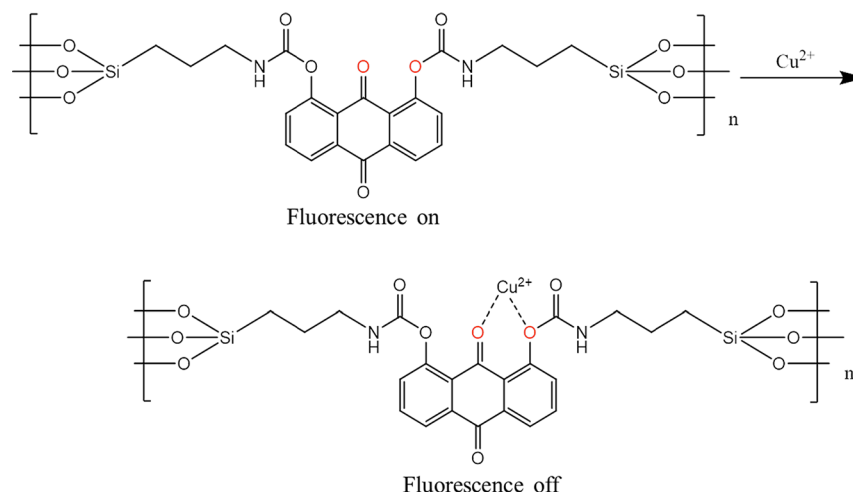
Scheme 3. The Possible Complex Mechanism between DHAQ-PMOs and Cu²⁺

Figure 10. (a) XPS survey spectrum, (b) C 1s, (c) O 1s, (d) Si 2p, (e) N 1s, and (f) Cu 2p spectra of the coordination of DHAQ-PMO-10 with Cu²⁺.

between HOMO and LUMO (2.8584 eV) is lower than the energy gap of DHAQ between HOMO and LUMO (3.3662 eV), which means that the whole system of DHAQ-Cu²⁺ is more stable than that of DHAQ. This phenomenon provides a strong evidence for the formation of a complex between DHAQ and Cu²⁺. We also calculated the possible binding modes of DHAQ-Si and Cu²⁺ listed in Table S3. The results indicated that other binding modes are not stable enough. Based on these results, the mechanism of recognizing Cu²⁺ may be the coordination interaction between Cu²⁺ and two oxygen atoms, i.e., one oxygen from the hydroxyl group and another from the carbonyl group of DHAQ (Scheme 3).

X-ray photoelectron spectrum (XPS) experiments were performed to analyze the elements and chemical bonds in DHAQ (Figure S13), DHAQ-Si (Figure S14), and DHAQ-PMO-10 (Figure S15), respectively. For DHAQ, the survey spectrum (Figure S13a) shows that there exist C and O elements. And the C 1s peaks at 284.7, 285.9, and 287.2 eV belong to C−C/C=C (carbons in anthraquinone ring), C−O, and C=O bonds.[58,59] Peaks at 531.2 and 532.7 eV of O 1s

correspond to C=O and C−O bonds.[60] As for DHAQ-PMO-10 (Figure S15), there exist C, N, O, and Si elements. The C 1s peaks at 283.8, 284.6, 285.4, 286.0, and 287.0 eV belong to C−Si, C−C/C=C (carbons in anthraquinone ring), C−N, C−O, and C=O bonds.[61] The three peaks at 530.8, 531.9, and 532.9 eV confirm the presence of C=O, C−O, and Si−O bonds in the O 1s spectrum.[62] The N 1s peaks at 399.3 and 402.2 eV are attributed to N−C and N−C=O bonds.[63] The Si 2p peaks at 102.0 and 103.4 eV belong to Si−C and Si−O bonds.[61] And DHAQ-Si has the same elements and chemical bonds as those of DHAQ-PMO-10 (Figure S14). The above results demonstrate that DHAQ molecules are embedded into the silica framework of the PMOs in the molecular level.

XPS spectra of the coordination of DHAQ and DHAQ-PMO-10 with Cu²⁺ are shown in Figure S16 and Figure 10, respectively. As we can see from the O 1s spectrum of Figure S16, there exist three peaks, which are located at 530.7, 531.4, and 532.3 eV, respectively, confirming the presence of Cu−O, C=O, and C−O bonds.[64] For the Cu 2p spectrum, the peaks at 932.3 (Cu 2p₃/₂) and 952.1 eV (Cu 2p₁/₂) correspond to the
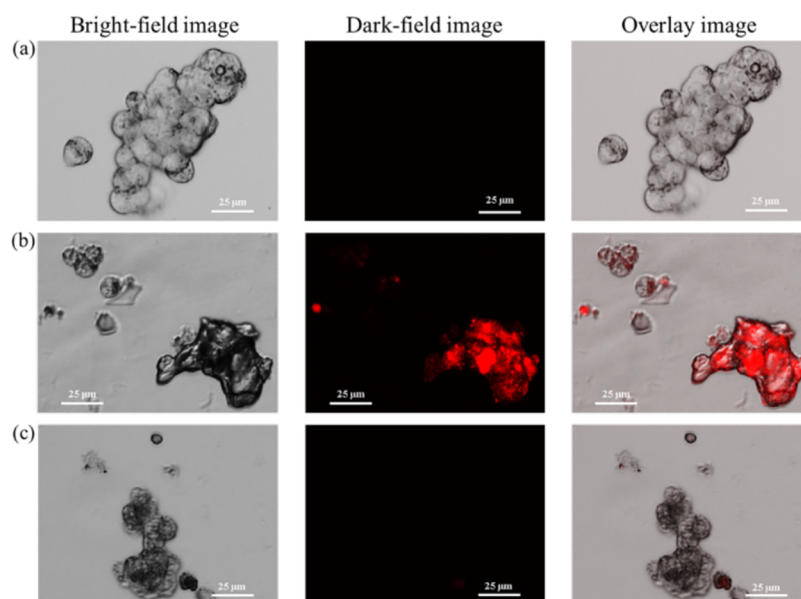
Figure 11. Confocal fluorescence microscope images of (a) HepG2 cells. (b) HepG2 cells incubated with DHAQ-PMO-10 (100 μg/mL) for 4 h. (c) HepG2 cells incubated with Cu^{2+} (10 μM) for another 4 h after incubation with DHAQ-PMO-10 for 4 h.

2p orbital of Cu^{2+}.[65] The satellites followed by Cu $2p_{3/2}$ prove the existence of the Cu−O bond.[66,67] For the coordination of DHAQ-PMO-10 with Cu^{2+}, there exist four peaks of the O 1s spectrum, which belong to Cu−O (530.2 eV), C═O (531.4 eV), C−O (532.2 eV), and Si−O (533.4 eV) bonds. The Cu 2p spectrum of the coordination of DHAQ-PMO-10 with Cu^{2+} (Figure 10) has the same peaks as that of DHAQ. These results prove that Cu^{2+} has coordinated with DHAQ and DHAQ-PMO-10, respectively.

2.8. Intracellular Sensing Application of DHAQ-PMO-10. To demonstrate the application value of DHAQ-PMO-10, a fluorescence imaging experiment was performed with HepG2 cells. The HepG2 cells were incubated with DHAQ-PMO-10 (100 μg/mL) for 4 h and then incubated with Cu^{2+} (10 μM) for another 4 h. The image of HepG2 cells incubated with DHAQ-PMO-10 show a bright red fluorescence. Very significant attenuation of the bright red fluorescence is exhibited with the addition of Cu^{2+} to HepG2 cells (Figure 11). The results show that DHAQ-PMO-10 can be used to detect Cu^{2+} in intracellular sensing.

3. CONCLUSIONS

In conclusion, a novel organic−inorganic hybrid periodic mesoporous material with DHAQ-Si and TEOS as the mixed silicon source and CTAB as the structure directing agent was synthesized in the ternary DES composed of ChCl/U/EG. DHAQ-PMOs have an obvious two-dimensional hexagonal structure. DHAQ itself has double fluorescence emission peaks at *ca.* 520 and 580 nm, respectively. After it is embedded into the mesoporous silica material, the silica framework provides a rigid environment to make the fluorescence properties of DHAQ more stable. And the luminescent efficiency of DHAQ is significantly improved, which makes DHAQ-PMOs as a fluorescence sensor detect Cu^{2+} with high selectivity and sensitivity in a wide pH range, and the limit of detection (LOD) can reach the nanomolar range. Moreover, the results of DFT and XPS further prove the coordination ability and interaction between DHAQ and Cu^{2+}. DHAQ-PMOs can also

detect Cu^{2+} in living cells by confocal fluorescence microscope experiments.

4. EXPERIMENTAL SECTION

4.1. Materials. All of the reagents and solvents were obtained from commercially available sources and used without further purification, unless otherwise specified. The DHAQ, triethylenediamine (TEDA), acetonitrile (CH_3CN), 4-(2-hydroxyethyl)-1-piperazineethanesulfonic acid (HEPES), ethylene glycol (EG), and cetyltrimethylammonium bromide (CTAB) were purchased from Shanghai Aladdin Biochemical Technology Co., Ltd. Tetraethylortho-silicate (TEOS) and anhydrous copper chloride were provided by Shanghai Macklin Biochemical Technology Co., Ltd. 3-Isocyanatopropyltriethox-ysilane (IPTES) was bought from Shanghai D&B Biological Science and Technology Co., Ltd. Dimethyl sulfoxide (DMSO), *n*-hexane, methanol, and ethanol were obtained from Tianjin Fuyu Reagent Company. Sodium hydroxide (flaky) was available from Sinopharm Chemical Reagent Co., Ltd. Choline chloride (ChCl) was obtained from Adamas Reagent Co., Ltd. Urea (U) was bought from Tianjin Guangcheng Chemical Reagent Co., Ltd.

4.2. Characterization. The ^1H NMR spectra were determined by means of a Bruker Avance III 400 MHz spectrometer, and DMSO-d_6 was used as the solvent. The HRMS spectra were recorded from an Agilent Q-TOF 6510 mass spectrometer. The FT-IR spectra were obtained on a Nicolet 700 FTIR spectrometer (Thermo-Fisher Scientific, Inc., Waltham, MA) with KBr flakes. Small-angle X-ray scattering (SAXS) was collected using the SAXSess mc^2 by Anton Paar; the sample−detector distance was set to 264.5 mm. TGA/DSC was carried out in a N_2 atmosphere using a METTLER TGA/DSC 3+ with a heating rate of 10 °C/min in the temperature range from room temperature to 800 °C. ^{29}Si magic angle spinning nuclear magnetic resonance (^{29}Si MAS NMR) spectra were obtained on a Bruker 400 MHz spectrometer (spin speed 10 kHz, prescan delay 6.5 μs). Scanning electron microscope (SEM) pictures were taken by S-4800 with an accelerating voltage of 5 kV. High-resolution

transmission electron microscope (HR-TEM) pictures were taken using an FEI Tecnai G2 F20 with an operating voltage of 200 kV. Nitrogen adsorption/desorption isotherms were acquired on a Micromeritics ASAP 2460-4MP surface area and porosity analyzer at 77 K. The entire UV−vis studies were carried out on an Agilent UV−vis−NIR spectrophotometer by using matched quartz cells. Fluorescence spectra were recorded by a Horiba FluoroMax-4 fluorescence spectrophotometer, which used a monochrome Xe lamp as the excitation source. Time-resolved fluorescence spectra were measured using an Edinburgh FLS920 fluorescence spectrophotometer. Intracellular fluorescence imaging was tested on a Leica SP8 laser scanning confocal microscope.

4.3. Synthesis. *4.3.1. The Preparation of the DHAQ Bridged Organosiloxane Precursor (DHAQ-Si).* DHAQ (0.24 g, 1 mmol) and IPTES (0.742 g, 3 mmol) were dissolved in dry DMSO (100 mL). And then TEDA (0.045 g, 0.4 mmol) was added to the solution. The mixture was refluxed at 105 °C for 48 h in a dry N_2 atmosphere. After the reaction, the solvent in the mixture was removed by rotary evaporation. The obtained solid was washed three times with *n*-hexane, after which DHAQ-Si was collected (yield, 68%). ^{1}H NMR (400 MHz, DMSO-d_6) δ (ppm) 7.67 (t, J = 7.9 Hz, 2H), 7.57 (d, J = 7.3 Hz, 2H), 7.24 (d, J = 8.3 Hz, 2H), 5.79 (t, J = 5.9 Hz, 2H), 3.84−3.57 (m, 12H), 2.93 (dd, J = 12.9, 6.6 Hz, 4H), 1.40 (d, J = 7.2 Hz, 4H), 1.20−1.04 (m, 18H), 0.54−0.47 (m, 4H) (Figure S17). HRMS found that the highest fragment peak at 469.28 belonged to [DHAQ-Si − IPTES − H_2O]. The small fragment peak at 891.50 was ascribed to [DHAQ-Si + 2DMSO + H]$^+$.[68] According to the *m/z* values of the two fragment peaks, the molecular weight of DHAQ-Si was 734.29 (Figure S18).

4.3.2. The Synthesis of Inorganic Mesoporous Materials with Different Contents of CTAB in the Ternary DES. First, ChCl (3.5 g, 0.025 M), U (3 g, 0.05 M), and EG (2.8 mL, 0.05 M) were mixed and stirred vigorously for 30 min at 80 °C until a uniform and transparent liquid was formed, and stirring was continued for 30 min to stabilize the DES. Then, CTAB (1, 2, 3, 4, 5, and 6 g), as the structure directing agent, was added to the DES, respectively, and stirred vigorously. Next, 5 mL of TEOS was added to the solution drop by drop. After heating and stirring the above solution for 2 h, 3 mL of 40% NaOH was added to make the pH of the solution reach 10, and heating was turned off. The solution was transferred to a Teflon-lined autoclave after the solution cooled to room temperature. The autoclave was put in an oven and reacted at 120 °C for 12 h. After cooling to room temperature, the product was filtered, washed alternately with ethanol and water three times, and dried in a vacuum to obtain the product.

4.3.3. The Preparation of DHAQ-PMOs. The synthesis method of DHAQ-PMOs was similar to the above method for inorganic mesoporous materials. Among them, the content of CTAB was determined to be 4 g. Mixed silicon sources of DHAQ-Si-*X* (*X* is the mass fraction of DHAQ-Si in the mixed compound, *X* = 0, 2, 5, and 10%) and TEOS (5 mL) were added to the DES together. Finally, the surfactant template CTAB was removed by Soxhlet extraction for 20 days using ethanol as the extract solvent.

4.3.4. Cell Culture and Fluorescence Imaging. The HepG2 cells were placed in Dulbecco's modified Eagle's medium (DMEM) containing 10% fetal bovine serum and cultured in an incubator at 37 °C with 5% CO_2 and 95% air. For fluorescence imaging, the cells were seeded in six-well plates at

a density of 1×10^5 cells/mL and cultured in DMEM containing 10% fetal bovine serum at 37 °C and 5% CO_2 for 24 h. Then DHAQ-PMO-10 (100 μg/mL) was added and cultured for 4 h. Then Cu^{2+} (10 μM) was added and cultured for another 4 h. All of these were washed with a PBS buffer. Photographs were obtained by a laser confocal microscope.

■ ASSOCIATED CONTENT

ⓢ Supporting Information

The Supporting Information is available free of charge at https://pubs.acs.org/doi/10.1021/acsomega.2c01944.

FTIR spectra, TGA/DSC curves, ^{1}H NMR of DES, UV−vis absorption and fluorescence emission spectra, fluorescence decay curves, fluorescence lifetimes and quantum yields, LOD of some sensors, DFT results, XPS spectra, and ^{1}H NMR and HRMS of the compound (PDF)

■ AUTHOR INFORMATION

Corresponding Author

Shuhua Han − *Key Lab of Colloid and Interface Chemistry Ministry of Education, School of Chemistry and Chemical Engineering, Shandong University, Jinan 250100, P.R. China;* ◎ orcid.org/0000-0002-9625-8916; Email: shuhhan@sdu.edu.cn

Author

Zhi Li − *Key Lab of Colloid and Interface Chemistry Ministry of Education, School of Chemistry and Chemical Engineering, Shandong University, Jinan 250100, P.R. China*

Complete contact information is available at: https://pubs.acs.org/10.1021/acsomega.2c01944

Notes

The authors declare no competing financial interest.

■ ACKNOWLEDGMENTS

■ REFERENCES

(1) Gérardin, C.; Reboul, J.; Bonne, M.; Lebeau, B. Ecodesign of ordered mesoporous silica materials. *Chem. Soc. Rev.* **2013**, *42*, 4217−4255.

(2) Kaczmarek, A. M.; Abednatanzi, S.; Esquivel, D.; Krishnaraj, C.; Jena, H. S.; Wang, G.; Leus, K.; Van Deun, R.; Romero-Salguero, F. J.; Voort, P. V. D. Amine-containing (nano-) Periodic Mesoporous Organosilica and its application in catalysis, sorption and luminescence. *Microporous Mesoporous Mater.* **2020**, *291*, 109687.

(3) Azizi, N.; Edrisi, M.; Abbasi, F. Mesoporous silica SBA-15 functionalized with acidic deep eutectic solvent: A highly active heterogeneous N-formylation catalyst under solvent-free conditions. *Appl. Organomet. Chem.* **2018**, *32*, No. e3901.

(4) Esquivel, D.; Amaro-Gahete, J.; Caballero-Casero, N.; Jiménez-Sanchidrián, C.; Ruiz, J. R.; Rubio, S.; Van Der Voort, P.; Romero-Salguero, F. J. Tailoring bifunctional periodic mesoporous organosilicas for cooperative catalysis. *ACS Appl. Nano Mater.* **2020**, *3*, 2373−2382.

(5) Pal, N.; Sim, S.; Cho, E.-B. Multifunctional periodic mesoporous benzene-silicas for evaluation of CO_2 adsorption at standard temperature and pressure. *Microporous Mesoporous Mater.* **2020**, *293*, 109816.

(6) Mousavi, K. Z.; Yamini, Y.; Karimi, B.; Seidi, S.; Khorasani, M.; Ghaemmaghami, M.; Vali, H. Imidazolium-based mesoporous

organosilicas with bridging organic groups for microextraction by packed sorbent of phenoxy acid herbicides, polycyclic aromatic hydrocarbons and chlorophenols. *Microchim. Acta* **2019**, *186*, 239−248.

(7) Lee, S. H.; Park, S. S.; Parambadath, S.; Ha, C.-K. Sulphonic acid functionalized periodic mesoporous organosilica with the bridged bissilylated urea groups for high selective adsorption of cobalt ion from artificial seawater. *Microporous Mesoporous Mater.* **2016**, *226*, 179−190.

(8) Attia, M. F.; Akasov, R.; Alexis, F.; Whitehead, D. C. Polymer-scaffolded synthesis of periodic mesoporous organosilica nanomaterials for delivery systems in cancer cells. *ACS Biomater. Sci. Eng.* **2020**, *6*, 6671−6679.

(9) Motealleh, A.; Dorri, P.; Kehr, N. S. Self-assembled monolayers of chiral periodic mesoporous organosilica as a stimuli responsive local drug delivery system. *J. Mater. Chem. B* **2019**, *7*, 2362−2371.

(10) Gao, M.; Xing, C.; Jiang, X.; Xu, L.; Li, P.; Hsiao, C. D. Highly selective fluorescence detection of Cu^{2+} based on Schiff base functionalized periodic mesoporous organosilicas. *Luminescence.* **2021**, *36*, 951−957.

(11) Kaczmarek, A. M.; Suta, M.; Rijckaert, H.; Abalymov, A.; Van Driessche, I.; Skirtach, A. G.; Meijerink, A.; Van Der Voort, P. Visible and NIR upconverting Er^{3+}-Yb^{3+} luminescent nanorattles and other hybrid PMO-inorganic structures for in vivo nanothermometry. *Adv. Funct. Mater.* **2020**, *30*, 2003101.

(12) Kubra, K. T.; Salman, M. S.; Hasan, M. N.; Islam, A.; Hasan, M. M.; Awual, M. R. Utilizing an alternative composite material for effective copper(II) ion capturing from wastewater. *J. Mol. Liq.* **2021**, *336*, 116325.

(13) Thirumalai, M.; Maheswari, M. A. Mesoporous silica monolith based colorimetric probes for Co^{2+} ions. *Mater. Lett.* **2021**, *300*, 130142.

(14) Waki, M.; Mizoshita, N.; Maegawa, Y.; Hasegawa, T.; Tani, T.; Shimada, T.; Inagaki, S. Enhanced fluorescence detection of metal ions using light-harvesting mesoporous organosilica. *Chem. − Eur. J.* **2012**, *18*, 1992−1998.

(15) Qiu, X.; Han, S.; Gao, M. Highly sensitive and selective detection of Cu (ii) by periodic mesoporous rhodamine derivative-based organosilicas with crystal-like pore walls. *J. Mater. Chem. A* **2013**, *1*, 1319−1325.

(16) Qiu, X.; Han, S.; Hu, Y.; Gao, M.; Wang, H. Periodic mesoporous organosilicas for ultra-high selective copper (ii) detection and sensing mechanism. *J. Mater. Chem. A* **2014**, *2*, 1493−1501.

(17) Gao, M.; Han, S.; Hu, Y.; Zhang, L. Enhanced fluorescence in tetraylnitrilomethylidyne- hexaphenyl derivative-functionalized periodic mesoporous organosilicas for sensitive detection of copper(II). *J. Phys. Chem. C* **2016**, *120*, 9299−9307.

(18) Kaczmarek, A. M.; Van Der Voort, P. Chemical sensors based on nano-sized lanthanide-grafted periodic mesoporous organosilica hybrid materials. *J. Mater. Chem. C* **2019**, *7*, 8109−8119.

(19) Wang, J.; Lv, M.; Wang, Z.; Zhou, M.; Gu, C.; Guo, C. Highly sensitive and selective fluorescent detection of rare earth metal Sn(II) ion by organic fluorine Schiff base functionalized periodic mesoporous material in aqueous solution. *J. Photochem. Photobiol., A* **2015**, *309*, 37−46.

(20) Mei, R.; Shi, Y.; Zhang, S.; Hu, J.; Zhu, L.; Gan, J.; Cai, L.; Ding, Z. Biotransformation of 1,8-dihydroxyanthraquinone into peniphenone under the fermentation of aleurodiscus mirabilis. *ACS Omega* **2020**, *5*, 33380−33386.

(21) Yan, X.-J.; Gao, Y.-Y.; Liu, H.-B.; Qiao, X.; Xie, C.-Z.; Li, Q.-Z.; Gao, W.-Z.; Sun, H.-B.; Xu, J.-Y. A novel double target fluorescence probe for Al^{3+}/Mg^{2+} detection with distinctively different responses and its applications in cell imaging. *Spectrochim. Acta, Part A* **2021**, *261*, 120067.

(22) Yadav, P.; Laddha, H.; Agarwal, M.; Kushwaha, H. S.; Gupta, R. Studies on 1,8-naphthalimide derivative as a robust multi-responsive receptor for an array of low cost microanalytical techniques for selective prompt and on-site recognition of duplicitous fluoride in semi-aqueous medium. *J. Fluorine Chem.* **2021**, *249*, 109858.

(23) Zhang, Y.-P.; Niu, W.-Y.; Ma, C.-M.; Yang, Y.-S.; Guo, H.-C.; Xue, J.-J. Fluorogenic recognition of Zn^{2+}, Cd^{2+} by a new pyrazoline-based multi-analyte chemosensor and its application in live cell imaging. *Inorg. Chem. Commun.* **2021**, *130*, 108735.

(24) Abbott, A. P.; Capper, G.; Davies, D. L.; Rasheed, R. K.; Tambyrajah, V. Novel solvent properties of choline chloride/urea mixtures. *Chem. Commun.* **2003**, *1*, 70−71.

(25) Tang, B.; Row, K. H. Recent developments in deep eutectic solvents in chemical sciences. *Monatsh. Chem.* **2013**, *144*, 1427−1454.

(26) Hayyan, M.; Hashim, M. A.; Hayyan, A.; Al-Saadi, M. A.; AlNashef, I. M.; Mirghani, M. E.; Saheed, O. K. Are deep eutectic solvents benign or toxic? *Chemosphere* **2013**, *90*, 2193−2195.

(27) Radošević, K.; Bubalo, M. C.; Srček, V. G.; Grgas, D.; Dragičević, T. L.; Redovniković, I. R. Evaluation of toxicity and biodegradability of choline chloride based deep eutectic solvents. *Ecotoxicol. Environ. Saf.* **2015**, *112*, 46−53.

(28) Zhao, B.-Y.; Xu, P.; Yang, F.-X.; Wu, H.; Zong, M.-H.; Lou, W.-Y. Biocompatible deep eutectic solvents based on choline chloride: characterization and application to the extraction of rutin from sophora japonica. *ACS Sustainable Chem. Eng.* **2015**, *3*, 2746−2755.

(29) Lee, D. W.; Jin, M. H.; Park, J. H.; Lee, Y. J.; Choi, Y. C.; Park, J.; Chun, D. H. Alcohol and water free synthesis of mesoporous silica using deep eutectic solvent as a template and solvent and its application as a catalyst support for formic acid dehydrogenation. *ACS Sustainable Chem. Eng.* **2018**, *6*, 12241−12250.

(30) Ferreira, V. R. A.; Azenha, M. A.; Pinto, A. C.; Santos, P. R. M.; Pereira, C. M.; Silva, A. F. Development of mesoporous polysaccharide/sol-gel composites with two different templating agents: Surfactants and choline chloride-based deep eutectic solvents. *Express Polym. Lett.* **2019**, *13*, 261−275.

(31) Biglari, M.; Shirini, F.; Mahmoodi, N. O.; Zabihzadeh, M.; Mashhadinezhad, M. A choline chloride-based deep eutectic solvent promoted three-component synthesis of tetrahydrobenzo[b]pyran and pyrano[2,3-d] pyrimidinone (thione) derivatives. *J. Mol. Struct.* **2020**, *1205*, 127652.

(32) Jurić, T.; Uka, D.; Holló, B. B.; Jović, B.; Kordić, B.; Popović, B. M. Comprehensive physicochemical evaluation of choline chloride-based natural deep eutectic solvents. *J. Mol. Liq.* **2021**, *343*, 116968.

(33) Bai, F.; Hua, C.; Li, J. Separation of benzene-cyclohexane azeotropes via extractive distillation using deep eutectic solvents as entrainers. *Processes* **2021**, *9*, 336−348.

(34) Zhu, J.; Shao, H.; Feng, L.; Lu, Y.; Meng, H.; Li, C. Absorptive separation of HCl gas by choline chloride-based deep eutectic solvents. *J. Mol. Liq.* **2021**, *341*, 116928.

(35) Zhu, S.; Li, H.; Zhu, W.; Jiang, W.; Wang, C.; Wu, P.; Zhang, Q.; Li, H. Vibrational analysis and formation mechanism of typical deep eutectic solvents: An experimental and theoretical study. *J. Mol. Graphics Modell.* **2016**, *68*, 158−175.

(36) Timin, A. S.; Rumyantsev, E. V.; Solomonov, A. V.; Musabirov, I. I.; Sergeev, S. N.; Ivanov, S. P.; Berlier, G.; Balantseva, E. Preparation and characterization of organo-functionalized silicas for bilirubin removal. *Colloids Surf., A* **2015**, *464*, 65−77.

(37) Jangir, A. K.; Mandviwala, H.; Patel, P.; Sharma, S.; Kuperkar, K. Acumen into the effect of alcohols on choline chloride: L-lactic acid-based natural deep eutectic solvent (NADES): A spectral investigation unified with theoretical and thermophysical characterization. *J. Mol. Liq.* **2020**, *317*, 113923.

(38) Le Thi, T. X.; Tran, H. L.; Cu, T. S.; Ho, S. L. Separation and enrichment of omega 3, 6, and 9 fatty acids from the by-products of vietnamese basa fish processing using deep eutectic solvent. *J. Chem.* **2018**, *2018*, 1−10.

(39) Deng, R.; Sun, Y.; Bi, H.; Dou, H.; Yang, H.; Wang, B.; Tao, W.; Jiang, B. Deep eutectic solvents as tuning media dissolving Cu^+ used in facilitated transport supported liquid membrane for ethylene/ethane separation. *Energy Fuels* **2017**, *31*, 11146−11155.

(40) Li, Q.; Wang, J.; Lei, N.; Yan, M.; Chen, X.; Yue, X. Phase behaviours of a cationic surfactant in deep eutectic solvents: from micelles to lyotropic liquid crystals. *Phys. Chem. Chem. Phys.* **2018**, *20*, 12175−12181.

(41) Parambadath, S.; Mathew, A.; Barnabas, M. J.; Ha, C. S. A pH-responsive drug delivery system based on ethylenediamine bridged periodic mesoporous organosilica. *Microporous Mesoporous Mater.* **2015**, *215*, 67−75.

(42) Peng, R.; Baltrusaitis, J.; Wu, C.-M.; Koodali, R. T. Pd-Ti-MCM-48 cubic mesoporous materials for solar simulated hydrogen evolution. *Int. J. Hydrogen Energy* **2015**, *40*, 905−918.

(43) Cychosz, K. A.; Guillet-Nicolas, R.; García-Martínez, J.; Thommes, M. Recent advances in the textural characterization of hierarchically structured nanoporous materials. *Chem. Soc. Rev.* **2017**, *46*, 389−414.

(44) Abbas, S. H.; Adam, F.; Muniandy, L. Green synthesis of MCM-41 from rice husk and its functionalization with nickel(II) salen complex for the rapid catalytic oxidation of benzyl alcohol. *Microporous Mesoporous Mater.* **2020**, *305*, 110192.

(45) Lopes, J. G. S.; Santos, P. S. The SERS spectrum of 1,2-diaminoanthraquinone studied on silver colloid. *J. Mol. Struct.* **2005**, *744-747*, 75−78.

(46) Dong, Y.; Wang, W.; Zhong, C.; Shi, J.; Tong, B.; Feng, X.; Zhi, J.; Dong, Y. Investigating the effects of side chain length on the AIE properties of water-soluble TPE derivatives. *Tetrahedron Lett.* **2014**, *55*, 1496−1500.

(47) Hao, Y.; Nguyen, K. H.; Zhang, Y.; Zhang, G.; Fan, S.; Li, F.; Guo, C.; Lu, Y.; Song, X.; Qu, P.; Liu, Y.-N.; Xu, M. A highly selective and ratiometric fluorescent probe for cyanide by rationally altering the susceptible H-atom. *Talanta* **2018**, *176*, 234−241.

(48) Shivraj, S.; Siddlingeshwar, B.; Kirilova, E. M.; Belyakov, S. V.; Divakar, D. D.; Alkheraif, A. A. Photophysical properties of benzanthrone derivatives: effect of substituent, solvent polarity and hydrogen bonding. *Photochem. Photobiol. Sci.* **2018**, *17*, 453−464.

(49) Tarai, A.; Huang, M.; Das, P.; Pan, W.; Zhang, J.; Gu, Z.; Yan, W.; Qu, J.; Yang, Z. ICT and AIE characteristics two cyano-functionalized probes and their photophysical properties, DFT calculations, cytotoxicity, and cell imaging applications. *Molecules* **2020**, *25*, 585−598.

(50) Zhou, A.; Han, S. An "off-on-off" fluorescence chemosensor for the sensitive detection of Cu^{2+} in aqueous solution based on multiple fluorescence emission mechanisms. *Analyst* **2021**, *146*, 2670−2678.

(51) Mohandoss, S.; Sivakamavalli, J.; Vaseeharan, B.; Stalin, T. Host-guest molecular recognition based fluorescence On-Off-On chemosensor for nanomolar level detection of Cu^{2+} and $Cr_2O_7^{2-}$ ions: Application in XNOR logic gate and human lung cancer living cell imaging. *Sens. Actuators, B* **2016**, *234*, 300−315.

(52) Li, Y.-J.; Wang, L.; Yan, B. Photoactive lanthanide hybrids covalently bonded to functionalized periodic mesoporous organosilica (PMO) by calix[4]arene derivative. *J. Mater. Chem.* **2011**, *21*, 1130−1138.

(53) Ye, B.-C.; Yin, B.-C. Highly sensitive detection of mercury(II) ions by fluorescence polarization enhanced by gold nanoparticles. *Angew. Chem., Int. Ed.* **2008**, *47*, 8386−8389.

(54) Poór, M.; Kunsági-Máté, S.; Matisz, G.; Li, Y.; Czibulya, Z.; Peles-Lemli, B.; Kőszegi, T. Interaction of alkali and alkaline earth ions with Ochratoxin A. *J. Lumin.* **2013**, *135*, 276−280.

(55) He, Y.; Tian, J.; Zhang, J.; Chen, S.; Jiang, Y.; Hu, K.; Zhao, Y.; Zhao, S. DNAzyme self-assembled gold nanorods-based FRET or polarization assay for ultrasensitive and selective detection of copper(II) ion. *Biosens. Bioelectron.* **2014**, *55*, 285−288.

(56) Wang, J.; Sun, R.; Hao, C.; Li, T.; Tian, Y.; Zhang, L. Influence of metal cations and cholesterol on lipid-amphotericin membrane. *Chem. Res. Chin. Univ.* **2017**, *33*, 447−453.

(57) Zhang, Y.; Li, Y.; Zhang, L. Fabricating multifunctional low-toxicity ratiometric fluorescent probe for individual detection of Cu^{2+}/glutamate and continuous sensing for glutamate via Cu^{2+}-based platform. *Spectrochim. Acta, Part A* **2021**, *259*, 119892.

(58) Maji, S. K.; Sreejith, S.; Mandal, A. K.; Ma, X.; Zhao, Y. Immobilizing gold nanoparticles in mesoporous silica covered reduced graphene oxide: A hybrid material for cancer cell detection through hydrogen peroxide sensing. *ACS Appl. Mater. Interfaces* **2014**, *6*, 13648−13656.

(59) Hu, C.; Zhu, Y.; Zhao, X. On-off-on nanosensors of carbon quantum dots derived from coal tarpitch for the detection of Cu^{2+}, Fe^{3+}, and L-ascorbic acid. *Spectrochim. Acta, Part A* **2021**, *250*, 119325.

(60) Du, H.; Xie, Y.; Zhang, H.; Chima, A.; Tao, M.; Zhang, W. Oxadiazole-functionalized fibers for selective adsorption of Hg^{2+}. *Ind. Eng. Chem. Res.* **2020**, *59*, 13333−13342.

(61) Liu, Z.; Hou, J.; Wang, X.; Hou, C.; Ji, Z.; He, Q.; Huo, D. A novel fluorescence probe for rapid and sensitive detection of tetracyclines residues based on silicon quantum dots. *Spectrochim. Acta, Part A* **2020**, *240*, 118463.

(62) Li, H.; Wang, C.; Yang, T.; Wang, Z.; Xia, M.; Zhang, M.; Liu, D.; Yuan, G. Mineralizing wood with chitosan-silica to enhance the flame retardant and physical-mechanical properties. *J. Sol-Gel Sci. Technol.* **2022**, DOI: 10.1007/s10971-022-05730-2.

(63) Gebremichael, G. T.; Kim, H.; Nisola, G. M.; Chung, W.-J. Asparagine anchored on mesoporous silica for Au (III) capture: Elucidation of adsorption-reduction mechanisms and their implications towards selective Au (III) recovery. *Appl. Surf. Sci.* **2021**, *567*, 150743.

(64) Rodríguez, B.; Oztürk, D.; Rosales, M.; Flores, M.; García, A. Antibiofouling thin-film composite membranes (TFC) by in situ formation of Cu-(m-phenylenediamine) oligomer complex. *J. Mater. Sci.* **2018**, *53*, 6325−6338.

(65) Balasubramanian, P.; Balamurugan, T. S. T.; Chen, S.-M.; Chen, T.-W. Facile synthesis of spinel-type copper cobaltite nanoplates for enhanced electrocatalytic detection of acetylcholine. *ACS Sustainable Chem. Eng.* **2019**, *7*, 7642−7651.

(66) Alhumaimess, M. S.; Essawy, A. A.; Kamel, M. M.; Alsohaimi, I. H.; Hassan, H. M. A. Biogenic-mediated synthesis of mesoporous Cu_2O/CuO nano-architectures of superior catalytic reductive towards nitroaromatics. *Nanomaterials* **2020**, *10*, 781−794.

(67) Jilani, A.; Abdel-Wahab, M. S.; Othman, M. H. D.; Sajith, V. K.; Alsharie, A. Sputtered CuO mono-phase thin films: Structural, compositional and spectroscopic linear/nonlinear optical character-istics. *Optik* **2017**, *144*, 207−218.

(68) Kim, H.; Na, Y. J.; Park, G. J.; Lee, J. J.; Kim, Y. S.; Lee, S. Y.; Kim, C. A novel selective colorimetric chemosensor for Cu^{2+} in aqueous solution. *Inorg. Chem. Commun.* **2014**, *49*, 68−71.